

Boundary-Conforming Free-Surface Flow Computations: Interface Tracking for Linear, Higher-Order and Isogeometric Finite Elements

Florian Zwicke*, Sebastian Eusterholz, Stefanie Elgeti

Chair for Computational Analysis of Technical Systems (CATS), RWTH Aachen University, 52056 Aachen, Germany
Center for Computational Engineering Science (CCES), RWTH Aachen University, 52056 Aachen, Germany

Abstract

The simulation of certain flow problems requires a means for modeling a free fluid surface; examples being viscoelastic die swell or fluid sloshing in tanks. In a finite-element context, this type of problem can, among many other options, be dealt with using an interface-tracking approach with the Deforming-Spatial-Domain/Stabilized-Space-Time (DSD/SST) formulation. A difficult issue that is connected with this type of approach is the determination of a suitable coupling mechanism between the fluid velocity at the boundary and the displacement of the boundary mesh nodes. In order to avoid large mesh distortions, one goal is to keep the nodal movements as small as possible; but of course still compliant with the no-penetration boundary condition. Standard displacement techniques are full velocity, velocity in a specific coordinate direction, and velocity in normal direction. In this work, we investigate how the interface-tracking approach can be combined with isogeometric analysis for the spatial discretization. If NURBS basis functions of sufficient order are used for both the geometry and the solution, both a continuous normal vector as well as the velocity are available on the entire boundary. This circumstance allows the weak imposition of the no-penetration boundary condition. We compare this option with an alternative that relies on strong imposition at discrete points. Furthermore, we examine several coupling methods between the fluid equations, boundary conditions, and equations for the adjustment of interior control point positions.

Keywords: Free-surface flow, Isogeometric Analysis, Interface tracking

1. Introduction

This paper can be placed in the field of free boundary problems. More specifically, it considers fluid flow problems where the computational domain is part of the solution — as in computational domains that contain a free surface. Examples considered here are sloshing tanks — under a seismic load, the liquid stored in a tank begins to slosh — and die swell — when a material melt exits the shape-giving die through which it has been pushed, it will expand.

Within a finite-element context, different methods are available to follow the position of the free surface throughout the computation [1, 2]. We generally distinguish between interface-capturing and interface-tracking methods. Examples for interface capturing methods are particle methods [3, 4], level-set [5, 6], volume of fluid [7, 8, 9, 10], or phase field [11, 12, 13, 14, 15, 16]. These approaches have in common that they use an additional function/marker to indicate the position of the free surface on an Eulerian background mesh. Examples for interface tracking are full Lagrangian or Arbitrary Lagrangian Eulerian (ALE) methods

*Corresponding author

Email addresses: zwicke@cats.rwth-aachen.de (Florian Zwicke), eusterholz@cats.rwth-aachen.de (Sebastian Eusterholz), elgeti@cats.rwth-aachen.de (Stefanie Elgeti)

NOTICE: This is the author's version of a work that was accepted for publication in *Computer Methods in Applied Mechanics and Engineering*. Changes resulting from the publishing process, such as editing, corrections, structural formatting, and other quality control mechanisms may not be reflected in this document. Changes may have been made to this work since it was submitted for publication.

August 15, 2017

[17]. Moreover, we would like to mention the Deforming-Spatial-Domain/Stabilized-Space-Time (DSD/SST) formulation [18], the interface tracking approach which has been used in this work.

For the considered test case of sloshing tanks, most methods mentioned above have been used in literature; as reviewed in [1]. In more recent publications, Grotle et al. employ the level-set method to compute turbulent sloshing [19]. A particle method is the basis of the analysis of a sloshing tank with two compartments performed in [20]. The die swell test case is an example with moderate deformations and no topological changes. It is therefore an ideal candidate for an interface tracking approach [21, 22, 23, 24, 25]. Nevertheless, also other methods are applicable. These include particle methods [26, 27, 28] and volume of fluid [29].

One major advancement in, but not limited to, the field of finite element methods is Isogeometric Analysis (IGA). Originally presented in [30], numerous works have been published on the subject in the last decade. The key idea of IGA is to replace the Lagrangian shape functions, which are generally used by finite element frameworks, by the geometry definition, as it would be used in Computer-Aided-Design (CAD) software. As detailed in [31], key advantages of the IGA approach are: (1) exact (as in CAD-conforming) geometry representation, (2) user-controlled smoothness and continuity of the basis, (3) in general higher accuracy per degree of freedom, (4) in general no node-to-node oscillations, etc. In the broad area of free boundary problems, Isogeometric Analysis has been applied in the context of the phase field method for the Cahn-Hilliard equations [32], brittle fracture [33], and topology optimization [34]. In connection with level-set, IGA has been utilized to compute the dam break problem [35, 36] or as a boundary indicator within the finite cell method [37]. Another free-surface-related application is the computation of wave resistance on a ship hull using the isogeometric boundary element method [38]. To the knowledge of the authors, IGA has not been utilized in conjunction with interface tracking of free surfaces.

The aim of this paper is therefore to define appropriate mesh displacement techniques for interface tracking of a free fluid boundary in an Isogeometric Analysis context. As compared to the classic, well-established methods in standard finite elements — displacement with the full fluid velocity, the normal fluid velocity, and the velocity in one specific coordinate direction — there will be one key difference: the unknown velocities and displacements no longer have a direct representation on the free surface. The reason is that, in IGA, the geometry is represented by non-uniform rational B-splines (NURBS) or other spline types. Their shape is controlled via control points. Usually, these control points will not coincide with the actual geometry.

The paper is structured as follows. Section 2 will introduce the governing equations for fluid flow, the no-penetration boundary condition for the free surface and the governing equations for the mesh adaptation. Classic numerical methods for their solution are reviewed in Section 3. Section 4 will then discuss how these equations can be interpreted in an IGA context. Two numerical examples — sloshing tank and die swell, both in 2D — will be presented in Section 5.

2. Governing equations for the free-boundary value problem of free-surface flow

For free-surface flow, three types of equations are relevant: (1) the Navier-Stokes equations in combination with an appropriate constitutive equation govern the fluid flow, (2) the displacement of the free surface, which is governed by the no-penetration boundary condition, and (3) the equations governing the possible displacement of interior parts of the domain in order to maintain validity of the mesh. This section will introduce those three equations in the form in which they have been used for the test cases shown in Section 5.

2.1. Governing equations for fluid flow: The Navier-Stokes equations

In the generic incompressible and isothermal fluid flow problem the unknowns are the velocity, $\mathbf{u}(\mathbf{x}, t)$, and the pressure, $p(\mathbf{x}, t)$. The computational domain at each instant in time, denoted by Ω_t , is a subset of \mathbb{R}^{nsd} , where nsd is the number of space dimensions. Then at each point in time $t \in [0, T]$, the flow problem is governed by the Navier-Stokes equations, which in our notation read:

$$\rho \left(\frac{\partial \mathbf{u}}{\partial t} + \mathbf{u} \cdot \nabla \mathbf{u} - \mathbf{f} \right) - \nabla \cdot \boldsymbol{\sigma} = \mathbf{0} \quad \text{on } \Omega_t, t \in [0, T], \quad (1)$$

$$\nabla \cdot \mathbf{u} = 0 \quad \text{on } \Omega_t, t \in [0, T], \quad (2)$$

with ρ as the density of the fluid. We consider only Newtonian fluids, meaning that the stress tensor $\boldsymbol{\sigma}$ is defined as

$$\boldsymbol{\sigma}(\mathbf{u}, p) = -p\mathbf{I} + 2\mu\boldsymbol{\varepsilon}(\mathbf{u}), \quad (3)$$

with

$$\boldsymbol{\varepsilon}(\mathbf{u}) = \frac{1}{2}(\nabla \mathbf{u} + (\nabla \mathbf{u})^T), \quad (4)$$

where μ denotes the dynamic viscosity. \mathbf{f} includes all external body forces with respect to the unit mass of fluid. Note that the spatial domain is time-dependent, which is indicated by subscript t .

For creeping flows (i.e., Reynolds number $\ll 1$), the advective term in the Navier-Stokes equations is often neglected, giving rise to the Stokes equations:

$$\rho \left(\frac{\partial \mathbf{u}}{\partial t} - \mathbf{f} \right) - \nabla \cdot \boldsymbol{\sigma} = \mathbf{0} \quad \text{on } \Omega_t, t \in [0, T], \quad (5)$$

$$\nabla \cdot \mathbf{u} = 0 \quad \text{on } \Omega_t, t \in [0, T]. \quad (6)$$

The constitutive equations for Newtonian fluids remain the same as above.

In the transient case, a divergence-free velocity field for the whole computational domain is needed as an initial condition:

$$\mathbf{u}(\mathbf{x}, 0) = \hat{\mathbf{u}}^0(\mathbf{x}) \quad \text{on } \Omega_t, t = 0. \quad (7)$$

In order to obtain a well-posed system, boundary conditions have to be imposed on the external boundary of Ω_t , denoted as Γ_t . Here, we distinguish between Dirichlet and Neumann boundary conditions given by:

$$\mathbf{u} = \hat{\mathbf{u}} \quad \text{on } \Gamma_u, t \in [0, T], \quad (8)$$

$$\mathbf{n} \cdot \boldsymbol{\sigma} = \hat{\mathbf{h}} \quad \text{on } \Gamma_h, t \in [0, T], \quad (9)$$

where $\hat{\mathbf{u}}$ and $\hat{\mathbf{h}}$ are prescribed velocity and stress values. Γ_u and Γ_h denote the Dirichlet and Neumann part of the boundary, forming a complementary subset of Γ_t , i.e., $\Gamma_u \cup \Gamma_h = \Gamma_t$ and $\Gamma_u \cap \Gamma_h = \emptyset$. \mathbf{n} refers to the outer normal vector on Γ_h .

2.2. Displacement of the free-surface: The no-penetration boundary condition

Depending on the specific application the full boundary Γ , or a portion thereof, can be defined as a free surface Γ_{free} . In an interface-tracking context, we want to ensure that the computational domain adapts to the fluid flow. The deformation of the free surface is governed by a no-penetration boundary condition, meaning that no fluid is allowed to cross the boundary. This condition will be fulfilled as long as the mass flux \dot{m} through Γ_{free} — and any given subset of Γ_{free} — is 0. The mass flux \dot{m} can be computed as:

$$\dot{m} = \int_{\Gamma^*} \rho(\mathbf{u} - \mathbf{v}) \cdot \mathbf{n} \, dx \stackrel{!}{=} 0, \quad \forall \Gamma^* \subseteq \Gamma_{free} \quad (10)$$

with ρ as fluid density, \mathbf{u} as fluid velocity and \mathbf{v} as mesh velocity.
Consequently, all choices for \mathbf{v} that comply with the kinematic boundary condition

$$\mathbf{v}(\mathbf{x}) \cdot \mathbf{n}(\mathbf{x}) = \mathbf{u}(\mathbf{x}) \cdot \mathbf{n}(\mathbf{x}) \quad (11)$$

are valid.

The straightforward choice is

$$\mathbf{v}(\mathbf{x}) = \mathbf{u}(\mathbf{x}). \quad (12)$$

This may however not always be the best choice. Equation (11) indicates that the tangential component of \mathbf{v} has no influence on the boundary shape — which is the actual result of the boundary displacement —, but may significantly influence the quality of the utilized computational mesh. Particularly applications with large tangential velocities — such as die swell — profit tremendously if the tangential velocity component is modified or even suppressed when computing the mesh velocity \mathbf{v} .

Behr [39] indicates several possibilities for boundary displacement resulting from Equation (11): displacement with the normal velocity component with $\mathbf{v} = (\mathbf{u} \cdot \mathbf{n})\mathbf{n}$ and displacement only in a specific direction \mathbf{d} (e.g., y -direction), i.e., $\mathbf{v} = \frac{(\mathbf{u} \cdot \mathbf{n})\mathbf{d}}{\mathbf{n} \cdot \mathbf{d}}$. The concept is detailed in [1].

2.3. Retaining mesh quality: Mesh update for inner nodes

As the boundary Γ_{free} is modified, usually the discretization of the interior of the domain needs to be adapted as well. For this purpose, we employ the Elastic Mesh Update Method (EMUM) [40]. In this method, the computational mesh is treated as an elastic body reacting to the boundary deformation applied to it. The linear elasticity equation is solved for the mesh displacement \mathbf{z} :

$$\nabla \cdot \boldsymbol{\sigma}_{mesh} = \mathbf{0}, \quad (13)$$

$$\boldsymbol{\sigma}_{mesh}(\mathbf{z}) = \lambda_{mesh} (\text{tr } \boldsymbol{\varepsilon}_{mesh}(\mathbf{z})) \mathbf{I} + 2\mu_{mesh} \boldsymbol{\varepsilon}_{mesh}(\mathbf{z}), \quad (14)$$

$$\boldsymbol{\varepsilon}_{mesh}(\mathbf{z}) = \frac{1}{2} (\nabla \mathbf{z} + (\nabla \mathbf{z})^T). \quad (15)$$

λ_{mesh} and μ_{mesh} — in structural mechanics the Lamé-parameters — have no physical meaning within the mesh deformation. They can be chosen freely for each element in order to control its respective stiffness.

The mesh update equations are solved at discrete points in time t on the domain Ω_t . We partition the boundary Γ into the disjoint parts Γ_{free} , Γ_{fixed} and Γ_{slip} with $\Gamma = \Gamma_{free} \cup \Gamma_{fixed} \cup \Gamma_{slip}$. Γ_{fixed} is the part of the boundary that does not change at all and Γ_{slip} is the part that allows tangential node movement. We obtain the boundary conditions

$$\mathbf{z} = \mathbf{0} \quad \text{on } \Gamma_{fixed}, \quad (16)$$

$$\mathbf{z} = \mathbf{z}_D \quad \text{on } \Gamma_{free}, \quad (17)$$

$$\mathbf{z} \cdot \mathbf{n} = 0 \quad \text{on } \Gamma_{slip}, \quad (18)$$

$$(\boldsymbol{\sigma}_{mesh}(\mathbf{z})\mathbf{n}) \cdot \mathbf{t}_l = 0 \quad \text{on } \Gamma_{slip}, \quad 1 \leq l \leq d-1, \quad (19)$$

where \mathbf{z}_D is the displacement on the free-surface boundary, \mathbf{n} is the surface normal vector and \mathbf{t}_i are a set of $d - 1$ linearly independent surface tangent vectors.

One should note that the slip boundary condition as it is described here can only preserve the shape of the boundary if it is completely straight.

3. Background on the employed simulation methods

3.1. The Deforming-Spatial-Domain/Stabilized-Space-Time (DSD/SST) formulation

The method we use for simulating our test cases is a variant of the deforming-spatial-domain/stabilized-space-time finite element formulation. As the name already indicates, it is a finite element method that is based on a space-time discretization — i.e., both the spatial domain and the temporal interval are discretized using finite elements. Similar to time-stepping, the space-time domain is usually subdivided into so-called space-time slabs (Figure 1). It is the use of space-time finite elements that is responsible for the main advantage of the method: the variational form of the governing equations can be written over a deforming domain. This allows mesh displacement in a very natural way, since the governing equations do not require any adjustments. Specifically, in contrast to standard ALE methods, the mesh velocity does not need to be included into the formulation as an advection velocity. Details on the method can be found in [18, 41]. Other extensions of DSD/SST are for example used by Tezduyar [42], Takizawa et al. [43, 44] and Zilian et al. [45]. Since the Navier-Stokes equations require stabilization when they are solved with the finite element method, we add Galerkin/Least-Squares (GLS) terms to the discretized weak form.

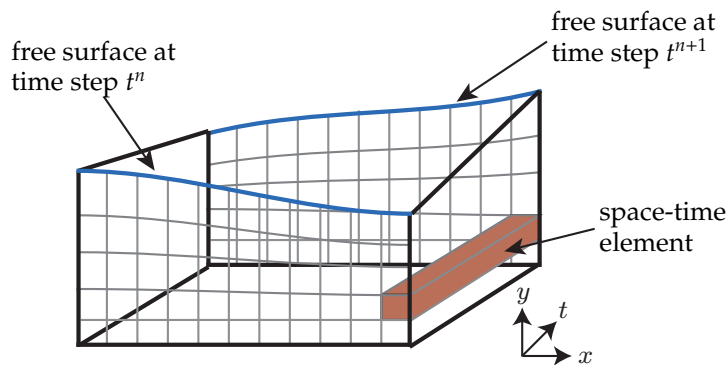


Figure 1: Illustration of a space-time slab tracking the deformation of the domain. In the front, we see the old time step, in back the new time step with a deformed domain.

3.2. Displacement of the free surface for standard finite elements

As discussed in Section 2.2, each point on the surface has to be displaced according to the rule that the normal component of the displacement velocity is equal to the normal component of the fluid velocity (cf. Equation (11)). For standard finite element discretizations, the finite element nodes lie directly on the surface; even more, they constitute the approximation of the surface. One approach to displacing the free surface is therefore to apply the chosen displacement rule (e.g., normal direction, vertical direction) directly to the finite element nodes. The procedure is illustrated in Figure 2. The challenge is the computation of the normal vector. Since the standard finite element shape functions are C^0 -continuous across element boundaries, that vector is not directly definable via the finite element approximation, but usually computed as a weighted average of the normals of surrounding element faces [46]. Other options are the computation from additional boundary descriptions that complement the finite element approximation [21, 23].

It is to be noted that this procedure will result in only an approximation of the no-penetration boundary condition (Equation (10)) as the displacement rule is not fulfilled exactly in between nodes (the normal

vector on a face is no longer constructable via the normal vectors at the corresponding nodes); however, an approximation is inevitable, as we only have an approximation of our geometry available in any case.

In summary, note that this method is tailored to linear temporal and spatial discretizations. It will perform poorly for higher-order shape functions. A requirement is that the nodes lie on the boundary. The accuracy of the method depends strongly on the type of approximation for the normal vector at the finite element nodes.

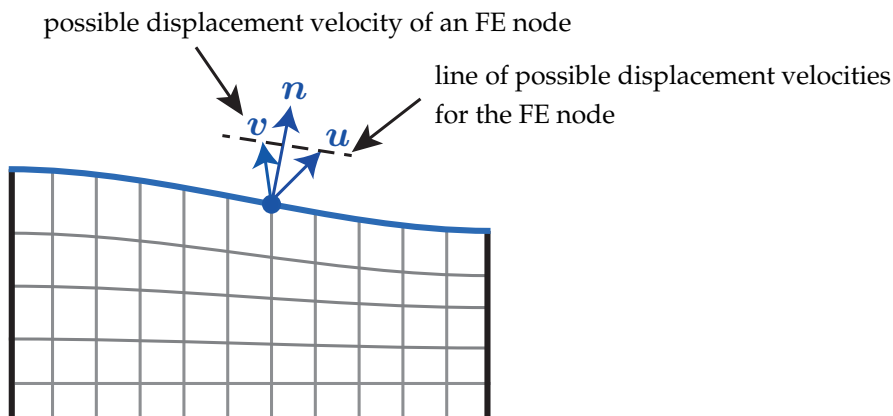


Figure 2: Illustration of possible displacement velocities for a given FE node on the free surface obeying the no-penetration boundary condition.

3.3. Isogeometric Analysis

Modern engineering design evolves around *Computer-Aided Design* (CAD) systems. As compared to drawing boards, modern CAD offers a significantly enhanced experience to the user. In engineering design, computer based geometry description is almost exclusively based on splines. More specifically, most CAD systems use Non-Uniform Rational B-Splines (NURBS) as a means of creating, communicating, and storing geometry information. From a strict engineering point of view, e.g., in a CAD/CAM context, this representation has proven to be very efficient.

3.3.1. Non-uniform rational B-splines (NURBS)

Detailed descriptions of NURBS and their properties can for example be found in [47, 48]. These books are also the basis for the following short description. NURBS belong to the category of parametric geometry representations. Their concept is derived for 1D geometrical entities, but can be extended to any spatial dimension. One-dimensional and two-dimensional splines are most common, however. In many cases, we encounter scenarios, where lower-dimensional spline entities are immersed in a higher-dimensional space. A NURBS curve \mathbf{C} (i.e., the 1D entity) is defined as

$$\mathbf{C}(\theta) = \sum_{i=1}^n R_{i,p}(\theta) \mathbf{P}_i, \quad (20)$$

where $R_{i,p}$ denote the NURBS basis functions (p being the polynomial degree) and \mathbf{P}_i are the coordinates of the control point i – which are always given in the global coordinate system \mathbf{x} . Note again that the dimension of \mathbf{x} can be 1 but also larger. n indicates the total number of control points. In the following, we will discuss the constituents of a NURBS curve in more detail.

The NURBS basis functions $R_{i,p}$ are rational polynomial functions with local support. The beginning and end of the interval, where a certain basis function is nonzero, is marked by a so-called knot. Knots

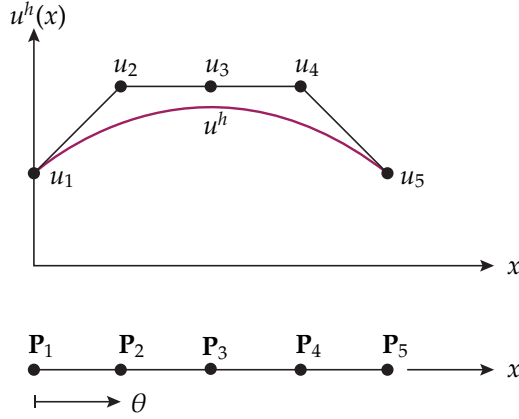


Figure 3: Approximation of an unknown function u on an isogeometric grid: The lower part of the picture shows a rod, which is represented using a quadratic NURBS with 5 control points. The upper part of the picture shows the representation of the unknown function u related to this grid. Instead of the five control points for the geometry, we now have five control variables that define the solution u^h .

are simply values in the parameter space. The range of $R_{i,p}$ is $[0, 1]$, however, the value of 1 is only rarely reached. One implication of this property is that the curve usually does not coincide with the control points.

The control points \mathbf{P}_i define the position and shape of the NURBS entity. They are arranged in a structured grid. Depending on the support of the corresponding basis function, which spans at most $p + 1$ elements, each control point influences the shape of the NURBS entity only in a limited area.

One important aspect of NURBS are their continuity properties. Between the basis and the distribution of control points, the user can control the continuity almost arbitrarily; constructing kinks or other discontinuities when needed, but profiting from high continuity otherwise. Specifically, a NURBS of polynomial degree p will be $p - 1$ times continuously differentiable when none of the knot values are repeated.

3.3.2. The isoparametric concept

Cottrell, Bazilevs and Hughes used NURBS to devise the concept of isogeometric analysis (IGA) [30, 31, 49]. In the spirit of the isoparametric concept, IGA utilizes the NURBS basis functions in order to represent both the geometry and the unknown solution. For the geometry, the already presented definition (20) is employed. The unknown function \mathbf{u} is then approximated in exactly the same fashion as:

$$\mathbf{u}^h = \sum_{i=1}^n R_{i,p}(\theta) \mathbf{u}_i. \quad (21)$$

The values \mathbf{u}_i are the control variables. These are the unknown values solved for in the finite element code. Note that just like the control points for the geometry, the values of the control variables are in general not coinciding with the solution; see Figure 3.

This idea not only essentially provides the capability to perform finite element analysis directly on CAD models, but it also profits from superior approximation properties of NURBS as compared to the polynomial shape functions used in the standard finite element method.

When used in free-surface flow, IGA is traditionally combined with an interface capturing approach. Recall that interface tracking, in contrast, means that the mesh will deform with the free surface. When IGA is applied to interface tracking, the challenge will be to find a proper displacement rule for the control points, which describe the free surface. Unlike in standard finite elements, the control points, which define the shape of the NURBS, are not located on the surface. The kinematic boundary condition (Equation (11)), however, needs to be fulfilled exactly there. The question will be, how to displace the control points in such a way, that the resulting curve displacement complies with the kinematic boundary condition?

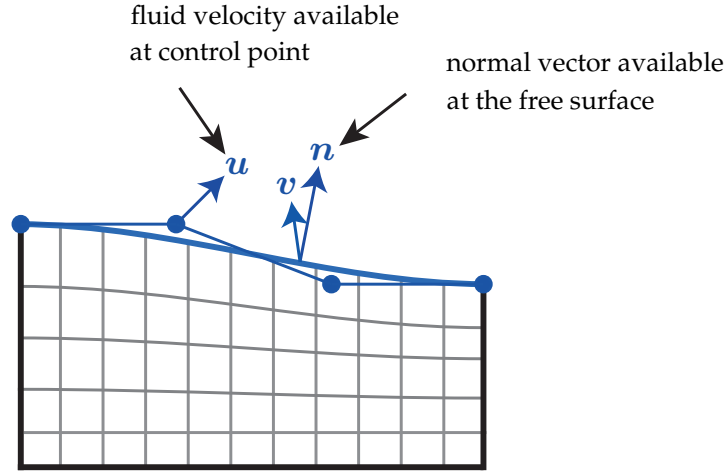


Figure 4: Illustration of possible displacement velocities for a given point on the free surface obeying the no-penetration boundary condition.

4. Implementation: How should the free surface be displaced?

As described in Section 2.2, the displacement of the free surface needs to fulfill the no-penetration boundary condition (Equation (10)), which can be rewritten into the kinematic boundary condition (Equation (11)). Even though setting the mesh displacement velocity equal to the fluid velocity will always fulfill this condition, it is vital to most application cases that other displacement schemes — e.g., in normal or in vertical direction — can be employed. Otherwise, tangential velocity components will have a negative influence on the mesh quality.

When this displacement concept is transferred to IGA, we face the problem that the unknowns (fluid and mesh velocity) are connected to the control points, whereas the kinematic boundary condition needs to hold for every point **on** the spline. The same holds for the normal vector, which can only be computed for the actual spline. At the control points, we have no notion of a normal vector.

Due to similar issues, weak imposition of Dirichlet boundary conditions has become a serious option for IGA [50]. Therefore, in addition to variants of the kinematic boundary condition (Equation (11)) — which in a sense can be considered a strong imposition of a boundary condition — methods based on the integral formulation of the no-penetration boundary condition (Equation (10)) — showing similarities to a weak imposition — might be beneficial.

In this paper, we propose two displacement methods for the free surface; one based on strong imposition and one on weak imposition. The first option entails moving the control points with normal vectors that are computed at the Greville abscissae. The second option considers the weak fulfillment of the no-penetration boundary condition — meaning that an additional equation system will need to be solved — in three different variants: (1) displacement in the surface normal direction, (2) displacement with the full velocity, and (3) displacement in a certain fixed direction.

4.1. Displacement based on the normal vector at the Greville abscissae

As detailed before, there is no notion of a normal vector at a control point. One point on the spline, whose normal vector might come close to a vector that might be considered a normal vector at a specific control point, is the normal vector at the corresponding Greville abscissa. The Greville abscissa is the point on the surface the control point converges to in case of refinement. The Greville abscissa can be computed as the average of the knot values relevant for a control point, excluding the first and last value [51]. Typically, this is also close to the point where the associated basis function is maximal (this is exactly fulfilled for uniform knot vectors). The normal vector at any parametric coordinate θ of a NURBS curve can then be

computed as [52]:

$$\mathbf{n}(\theta) = \begin{pmatrix} -t_y \\ t_x \end{pmatrix}, \quad \text{with tangent vector } \mathbf{t}(\theta) = \begin{pmatrix} t_x \\ t_y \end{pmatrix} = \frac{\mathbf{C}'(\theta)}{|\mathbf{C}'(\theta)|}. \quad (22)$$

The formula requires $\mathbf{C}'(\theta)$, the first derivative of the curve with respect to the local parameter θ , for the definition of which we refer to [47].

Based on the fluid velocity at any given control point \mathbf{P}_i , we define its displacement (or control point coordinate increment) $\Delta \mathbf{P}_i$ as:

$$\Delta \mathbf{P}_i := (\bar{\mathbf{u}}_i \cdot \bar{\mathbf{n}}_i) \bar{\mathbf{n}}_i \cdot \Delta t, \quad (23)$$

with $\bar{\mathbf{u}}_i$ and $\bar{\mathbf{n}}_i$ being the fluid velocity at control point i and the normal vector evaluated at the i^{th} Greville abscissa, both averaged over the time slab.

4.2. Displacement based on weak formulation of the kinematic boundary condition

We can also treat the no-penetration condition as a partial differential equation (PDE) on the boundary. We can solve this with the finite element method. Since the no-penetration condition provides just one scalar equation, it is not sufficient to solve for multiple boundary coordinate values in two- or three-dimensional space.

Multiple options are available to formulate a well-determined system of equations. To cover the different options, we will first treat the discretization of the equations in an abstract way by considering an operator $\mathcal{F}(\mathbf{u}, \mathbf{s})$ and the PDE

$$\mathcal{F}(\mathbf{u}, \mathbf{s}) = 0 \quad \text{on} \quad \Gamma_{free,t}, \quad t \in [0, T]. \quad (24)$$

In this equation, \mathbf{u} is the fluid velocity and \mathbf{s} is the boundary displacement relative to a reference configuration Ω_0 . We denote the free-surface portion of the boundary of Ω_t as $\Gamma_{free,t}$.

We introduce a spatial discretization space $\mathcal{I}_0 \subset C^0(\Gamma_{free,0})$. This is a finite-dimensional space that may be based on Lagrange or spline interpolation, depending on whether the standard finite element method or isogeometric analysis is used. We look at a single time slab $J = [t_k, t_{k+1}] \subseteq [0, T]$. We define a function

$$\tilde{\varphi} \in \mathcal{I}_0^d \otimes \mathbb{P}_1(J), \quad (25)$$

with spatial dimensionality d , such that

$$\tilde{\varphi} : \Gamma_{free,0} \times J \rightarrow \tilde{P} \quad \text{with} \quad \tilde{P} \subset \mathbb{R}^d. \quad (26)$$

We now choose $\tilde{\varphi}$ such that φ , defined by

$$\varphi(\mathbf{x}, t) = \begin{pmatrix} \tilde{\varphi}(\mathbf{x}, t) \\ \text{Id}_J(t) \end{pmatrix}, \quad (27)$$

$$\text{with} \quad \varphi : \Gamma_{free,0} \times J \rightarrow P_{free}, \quad (28)$$

is a homeomorphism. Here, P_{free} is the deformed space-time free-surface boundary, which can be related to $\Gamma_{free,t}$ by

$$P_{free} = \{(\mathbf{x}, t) \in \mathbb{R}^d \times J \mid \mathbf{x} \in \Gamma_{free,t}\}. \quad (29)$$

We use this to define a trial space \mathcal{S} and test space \mathcal{T} :

$$\mathcal{S} = \{s \circ \varphi^{-1} \mid s \in \mathcal{I}_0 \otimes \mathbb{P}_1(J)\}, \quad (30)$$

$$\mathcal{T} = \{w \circ \varphi^{-1} \mid w \in \mathcal{I}_0 \otimes \mathbb{P}_0(J)\}, \quad (31)$$

where \mathbb{P}_p is the space of polynomials of degree p . One should note that different polynomial degrees in time are used for these spaces. Specifically, the test space \mathcal{T} only includes functions that are constant in time.

We want the geometry description to be continuous over time slab boundaries. Therefore, we have to impose a temporal Dirichlet boundary condition on the lower level of the time slab for the discrete displacement field \mathbf{s}^h . This requires an adjusted trial space \mathcal{S}_s :

$$\mathcal{S}_s = \{\mathbf{s} \in \mathcal{S}^d \mid \mathbf{s}|_{t_k} = \mathbf{s}_k\}, \quad (32)$$

where \mathbf{s}_k with $\mathbf{s}_k \circ \varphi|_{t_k} \in \mathcal{I}_0^d$ is a given initial condition for the current time slab. The relationship between the discrete displacement field \mathbf{s}^h and the geometry is given by

$$\tilde{\varphi}^{-1}(\mathbf{x}, t) = \mathbf{x} - \mathbf{s}^h(\mathbf{x}, t) \quad \text{on } P_{free}. \quad (33)$$

This places a further restriction on \mathbf{s}^h , since only such choices are valid which allow φ to be a homeomorphism.

As mentioned before, the test space \mathcal{T} in (31) was designed to include only functions that are constant in time. In this way, it differs from the trial space \mathcal{S} and has a lower dimensionality. This is necessary, since the dimensionality of \mathcal{S}_s is also reduced. With the selected spaces, we get

$$d \cdot \dim \mathcal{T} = \dim \mathcal{S}_s, \quad (34)$$

which ensures that the number of equations will match the number of unknown displacement variables. We can now formulate the discretized weak form of the equation: Find $\mathbf{u}^h \in \mathcal{S}^d$ and $\mathbf{s}^h \in \mathcal{S}_s$ such that

$$\int_J \int_{\Gamma_{free,t}} w^h \mathcal{F}(\mathbf{u}^h, \mathbf{s}^h) \, d\mathbf{x} \, dt = 0 \quad (35)$$

for all $w^h \in \mathcal{T}$.

In order to form a closed system, these equations have to be combined with the fluid (Navier-Stokes) and mesh update (EMUM) equations.

We have so far kept the descriptions independent of the spatial dimensionality. However, while both two- and three-dimensional options for the operator \mathcal{F} are available, we will at this point stay in the two-dimensional realm. In this work, we investigate three possible choices for the operator \mathcal{F} .

A simple option is to move the mesh boundary exactly with the fluid velocity. We are going to call this option *equal movement* in the remainder. For this option, we set the mesh velocity as

$$\mathbf{v} = \mathbf{u} \quad (36)$$

$$\Leftrightarrow \frac{\partial \mathbf{s}}{\partial t} = \mathbf{u}. \quad (37)$$

We have seen best results with a variant of the equations that is formulated for a rotated coordinate system that is aligned with the boundary. This means that the equations are not formulated using horizontal and vertical parts, but using parts that are normal or tangential to the boundary. We will make use of a boundary tangential vector \mathbf{t} and boundary normal vector \mathbf{n} , which can both be interpreted as functions of the displacement field \mathbf{s} . The condition for equal mesh movement, formulated in normal and tangential directions, now reads

$$\frac{\partial \mathbf{s}}{\partial t} \cdot \mathbf{n} = \mathbf{u} \cdot \mathbf{n}, \quad (38)$$

$$\frac{\partial \mathbf{s}}{\partial t} \cdot \mathbf{t} = \mathbf{u} \cdot \mathbf{t}, \quad (39)$$

which yields the following choice for \mathcal{F} :

$$\mathcal{F}_1(\mathbf{u}, \mathbf{s}) = \frac{\partial \mathbf{s}}{\partial t} \cdot \mathbf{n}(\mathbf{s}) - \mathbf{u} \cdot \mathbf{n}(\mathbf{s}), \quad (40)$$

$$\mathcal{F}_2(\mathbf{u}, \mathbf{s}) = \frac{\partial \mathbf{s}}{\partial t} \cdot \mathbf{t}(\mathbf{s}) - \mathbf{u} \cdot \mathbf{t}(\mathbf{s}). \quad (41)$$

For flows with a strong velocity component tangential to the surface — e.g., die swell —, this option will lead to large mesh distortions: the mesh can be swept away!

The first equation for the equal movement is exactly the no-penetration condition that was formulated previously. A logical alternative option for the mesh movement results if we prevent mesh movement in the tangential direction. We call this *normal-direction movement*. The first equation (40) stays in place, and the second one changes to

$$\mathcal{F}_2(\mathbf{u}, \mathbf{s}) = \frac{\partial \mathbf{s}}{\partial t} \cdot \mathbf{t}(\mathbf{s}) \quad (42)$$

in this case.

This choice minimizes $\mathbf{v} = \partial \mathbf{s} / \partial t$, which may help in preserving mesh quality. Furthermore, it places no restrictions on the direction of \mathbf{n} or \mathbf{u} .

Finally, we can also restrict the mesh movement to an arbitrary *direction*. We still use (40) to fulfill the no-penetration condition, but we set the tangential movement according to a direction vector \mathbf{d} :

$$\mathcal{F}_2(\mathbf{u}, \mathbf{s}) = \frac{\partial \mathbf{s}}{\partial t} \cdot \mathbf{t}(\mathbf{s}) - \frac{\mathbf{u} \cdot \mathbf{n}(\mathbf{s})}{\mathbf{d} \cdot \mathbf{n}(\mathbf{s})} \mathbf{d} \cdot \mathbf{t}(\mathbf{s}). \quad (43)$$

Here, \mathbf{d} signifies a selected direction vector. Usually, \mathbf{d} will be defined as one of the unit coordinate vectors. However, it is required that $\mathbf{d} \cdot \mathbf{n} \neq 0$, implying that \mathbf{d} can never be tangential to the surface. Note that mesh quality will suffer for small values of $\mathbf{d} \cdot \mathbf{n}$. In contrast, for $\mathbf{d} \approx \mathbf{n}$, this definition of \mathcal{F} can preserve mesh quality over long stretches of time. In particular, this is due to the fact that a return to the initial boundary will always exactly recreate the initial boundary mesh (i.e., there can be no tangential sliding of control points over time). This stands in contrast to the displacement in normal direction.

For the case of pure vertical movement, which we have used in our examples, the simpler, but equivalent, equation

$$\mathcal{F}_2(\mathbf{u}, \mathbf{s}) = \frac{\partial \mathbf{s}_1}{\partial t} \quad (44)$$

can be used.

In the following section, the different displacement options will be applied to the test cases.

5. Test cases: How do the PDE-based and node-based displacements compare?

In order to compare and validate the new approaches to surface displacement, we have selected two common test cases. The first test case — a sloshing tank — features a damped periodic movement with a strong component orthogonal to the sloshing direction. The second test case — die swell — is also characterized by a movement orthogonal to the flow direction, however, in this case, the flow velocity features a strong tangential component.

5.1. Test case sloshing tank

The first test case considers a fluid enclosed in a tank with three straight walls at a 90-degree angle. As indicated in Figure 5, the tank has a dimensionless width of 1.0. The fluid — viscosity 0.01 and density 1000 — is initially in a non-equilibrium position. The initial free-surface position is described via its height $h(x) = 1 - 0.1 \cdot \cos(\pi x)$. The average height is 1.0. On all walls, a slip boundary condition is imposed. This means that the velocity is set to zero in the surface normal direction using a combination of Dirichlet and Neumann boundary conditions for the different components. Upon start of the simulation, the fluid will start to slosh, heading towards its equilibrium position at constant height. The sloshing is computed for a dimensionless time interval of 50. This corresponds to ten full sloshing cycles given a gravity constant of -1.0 .

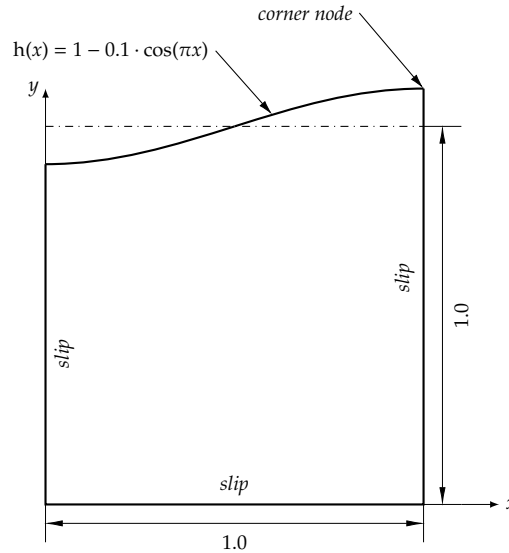


Figure 5: Sloshing tank: Setup of geometry, boundary and initial conditions.

For all standard finite element computations, we use a Q1Q1 (i.e., bilinear basis functions for both pressure and velocity interpolation spaces) structured mesh with 12 by 12 nodes (coarse) or 24 by 24 nodes (fine). The time step varies between 0.2 (coarse) and 0.1 (fine).

The IGA simulations are conducted with a coarse mesh containing 12 by 12 control points or a fine mesh containing 24 by 24 control points. In both cases, we consider a spline of degree 2. The element distribution in physical space is indicated in Figure 6.

For both — standard FEM and IGA — the initial position of the nodes / control points describing the free surface is computed by solving a least-squares fit problem.

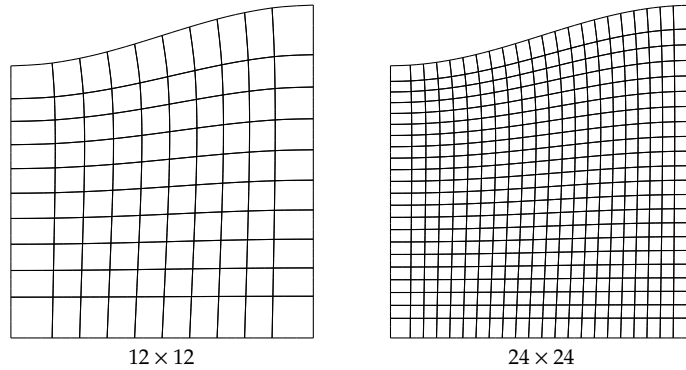


Figure 6: Meshes used for IGA simulations with $p = 2$. Elements are shown in physical space.

One standard means of comparison for this type of benchmark is the mass conservation. In general, when utilizing a finite element method, mass loss is expected. Figure 7 plots the mass conservation error \tilde{m} , defined as

$$\tilde{m}(t) := \left| \frac{m(t)}{m_0} - 1 \right| = \left| \frac{m(t)}{m(0)} - 1 \right|, \quad (45)$$

on a logarithmic scale. Here, $m(t)$ signifies the fluid mass in the tank, with m_0 as initial mass. The left plot shows results for the standard finite element method. Compared are (1) the traditional, node-based displacement in normal direction and (2) the PDE-based imposition in the variants full velocity, normal velocity and vertical velocity. The traditional version shows a mass loss that noticeably deviates from the ideal value of 0.0. Note that — via design — the PDE-based imposition of the no-penetration boundary condition preserves mass up to machine precision.

This observation still holds true for the IGA case displayed on the right plot. Again, the point-based variant — here, Greville points — leads to a mass loss, which is roughly nine orders of magnitude higher than the PDE-based versions. Note that for both plots, a comparison of the PDE methods among each other is not justifiable given how close the values are to machine precision.

In both plots, the simulations utilizing a displacement with the full fluid velocity break off, before they reach the final simulation time. This is due to the mesh becoming invalid (mesh tangling). This is again a substantiation of the claim that movement in a fully Lagrangian sense is in general not useful. In the IGA case, invalid meshes occur also for the Greville case.

In addition to mass conservation, the overall shape of the free surface is of interest. One possible indicator is the vertical position — $y(t)$ — of the northeast corner of the simulation domain plotted over time (cf. Figure 8 for the results on the fine meshes). For standard FEM, all versions lead to qualitatively similar results (top-left plot). Only a zoom (lower-left plot) reveals minor differences. For IGA — as for FEM — all PDE versions lead to similar results (top-right plot), where again only a zoom reveals minor variations (lower-right plot). However, the Greville version yields results that are in no relation to all other results.

So far, standard FEM and IGA were always regarded separately, since there are plenty of reasons for differing results — e.g. degree of interpolation, continuity across elements, imposition of boundary conditions — that go far beyond the task of mesh adaptation. Nevertheless — in the limit of fine temporal and spatial resolution —, the results for all variants are expected to converge towards one common solution. Since the exact solution is not available for comparison, it is difficult to judge the correctness of the respective

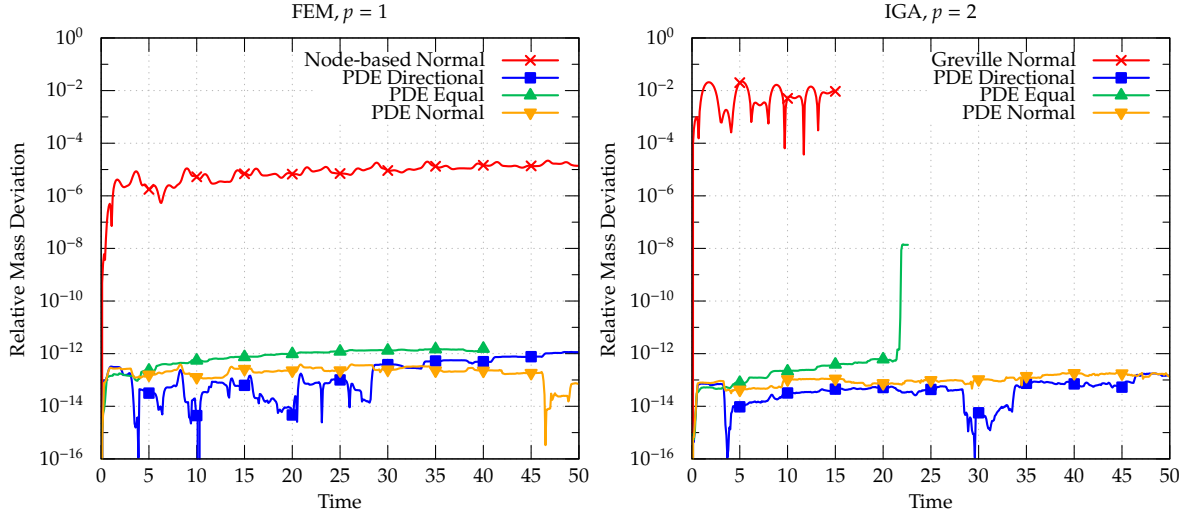


Figure 7: Mass conservation error $|m(t)/m_0 - 1|$ for different displacement methods of the free surface. On the left, the results for the standard finite element method are collected. The new, PDE-based approaches show a significant improvement of the mass conservation as compared to the traditional, node-based versions. On the right, the results for the IGA versions are displayed. Again, the PDE-versions preserve mass almost up to machine precision.

results. Still, it is possible to observe the results during mesh refinement. Figure 9 shows the results for standard FEM and IGA with PDE-based normal-direction mesh movement on the respective coarse and fine meshes. On the coarse meshes, the results show significant differences in both phase and amplitude. While it is impossible to say which variant is closer to the exact solution, the fact that the results are far more in agreement on the fine meshes indicates that both variants converge towards the same limit.

When using the total mass flux as a criterion for judging the quality of the method, both spatially and temporally local errors in the no penetration condition can be overlooked. For this reason, we introduce another error measure: the flux error \tilde{f} over the space-time boundary. This is defined as

$$\tilde{f} = \sqrt{\frac{\int_0^T \int_{\Gamma_{free,t}} |\mathbf{u} \cdot \mathbf{n} - \mathbf{v} \cdot \mathbf{n}|^2 \, dx \, dt}{\int_0^T \int_{\Gamma_{free,t}} dx \, dt}}. \quad (46)$$

For the example of an IGA simulation with directional movement, we show the flux error \tilde{f} for different mesh sizes and time step widths in Table 1. The table shows an almost perfect linear relationship between the flux error and the time step width. The influence of the mesh resolution only becomes relevant for extremely small time step widths, which are no longer practical. One should note that this error measure only considers the flux over the free surface, and not the quality of the overall solution. The finer mesh can still be expected to be beneficial for the flow solution.

Mesh \ Δt	$2.0 \cdot 10^{-1}$	$1.0 \cdot 10^{-1}$	$5.0 \cdot 10^{-2}$	$2.5 \cdot 10^{-2}$	$1.25 \cdot 10^{-2}$	$6.25 \cdot 10^{-3}$
12×12	0.009404	0.004748	0.002393	0.001229	0.000687	0.000482
24×24	0.009399	0.004743	0.002377	0.001191	0.000599	0.000307

Table 1: Table showing flux error \tilde{f} for different time step widths and mesh resolutions for an IGA simulation of the sloshing tank with directional free-surface movement.

With mass conservation and final result being in very similar ranges, up until now, it remains unclear which PDE-based mesh deformation version is the most suited for the application of sloshing tank. An

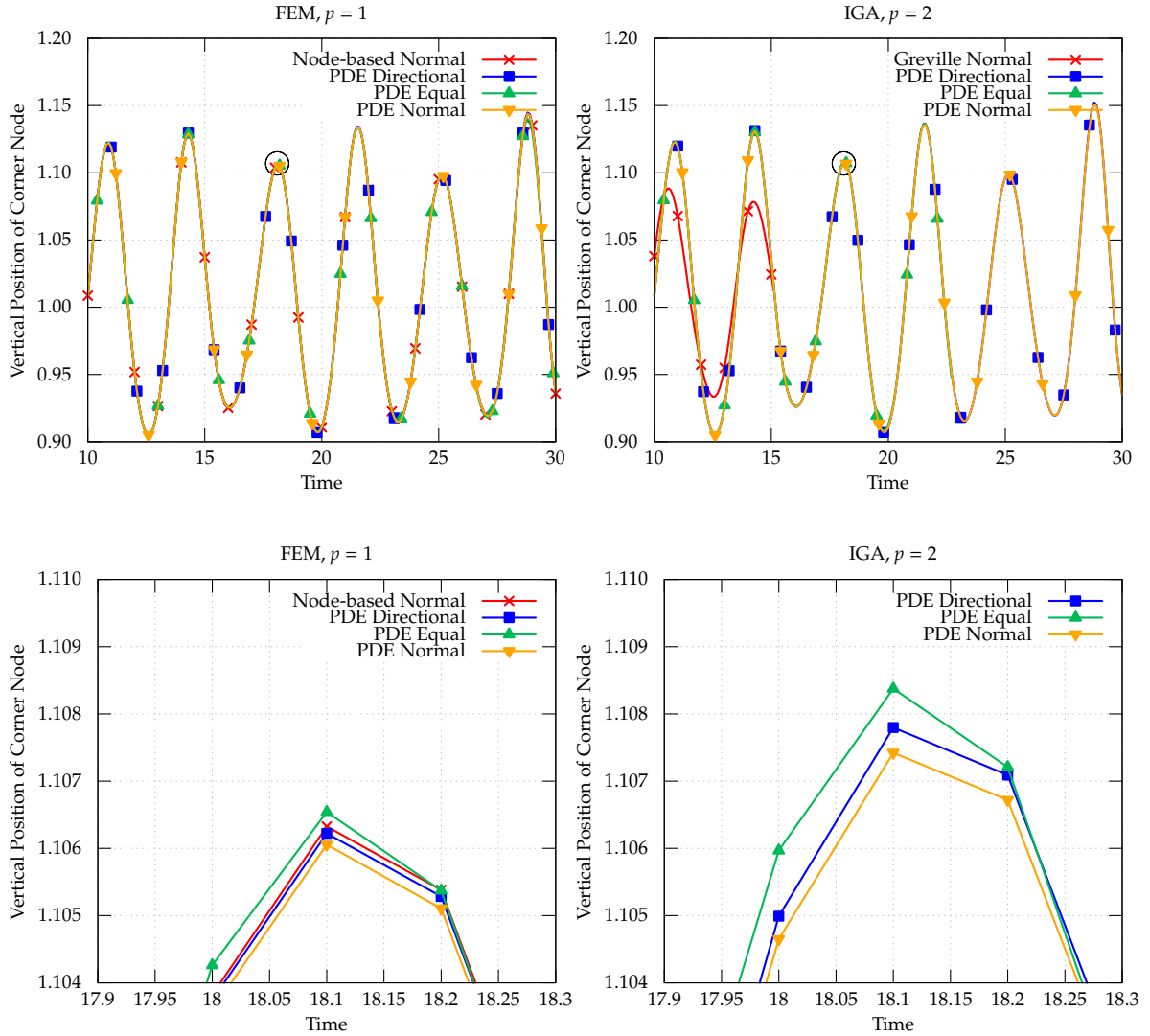


Figure 8: As an indicator of the free-surface shape, the vertical position of upper right corner of the computational domain is plotted over time for linear FEM (left) and quadratic IGA (right). The lower plots constitute a zoom on the respective upper plot. All simulations were conducted on the fine mesh.

answer can be found when comparing the mesh quality for the different versions. Here, the IGA variants will serve as an example, but all effects can be observed in the standard FEM meshes in the same way. Figures 10 through 13 show clear advantages of the PDE-based vertical displacement over all other versions. As already seen before, the Greville-based displacement leads to a free surface with a small kink, which is considered to be an invalid result (Figure 10). PDE-based normal (Figure 11) and PDE-based equal (Figure 13) displacement both have the disadvantage that they — to some extent — still allow for tangential displacement of nodes / control points. Over the course of several sloshing cycles, this inevitably leads to poor mesh quality — note the distorted elements — or even breakdown of the simulation. Only the PDE-based vertical displacement leads to a mesh displacement that can be carried out with no practical limit. All results were plotted for the coarse mesh for the sake of better readability, but hold in the same way for the fine mesh.

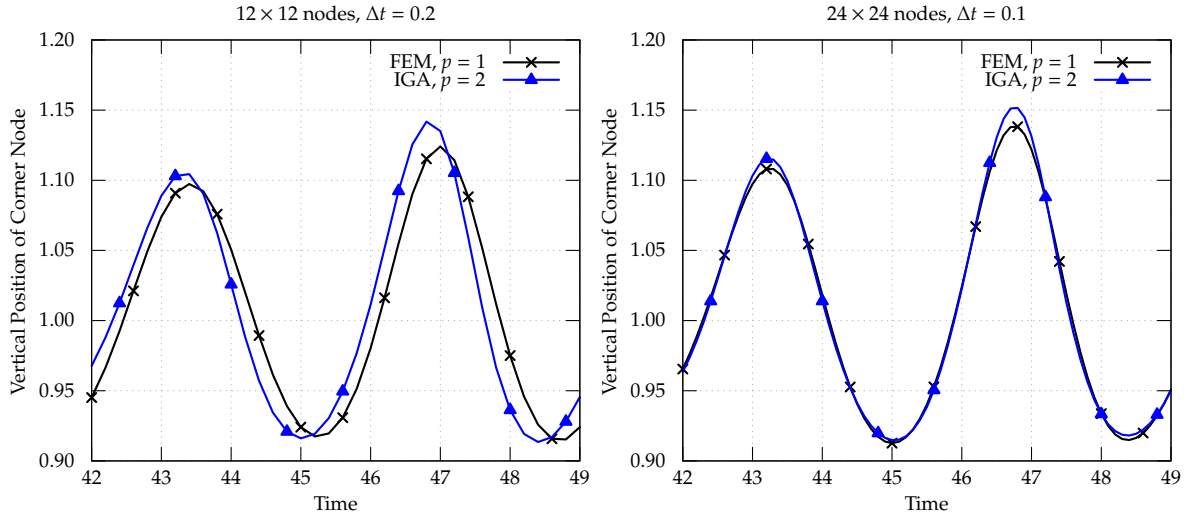


Figure 9: Comparison of linear FEM and quadratic order IGA simulations with PDE-based normal-direction movement on coarse mesh (left) and fine mesh (right). The meshes have been refined equally in spatial and temporal dimensions in order to keep the element size ratio roughly constant.

5.2. Test case die swell

The second test case considers the behavior of a fluid that exits a nozzle (cf. Figure 14 for the exact set-up). The Newtonian fluid — density 1.0 and viscosity 100000 — enters the nozzle from the left with a prescribed velocity of $\mathbf{u}(y) = (0.1(100 - y^2), 0)^T$. Gravity is neglected. The lower boundary is a symmetry boundary with a slip condition on the velocity. The top boundary is partially a wall — nozzle part — and partially a free surface. On the free-surface part, natural boundary conditions are used. This means that the stress on the boundary will be zero in surface normal direction. Due to the change in boundary condition on the top boundary from no-slip to free surface, the velocity profile restructures itself from parabolic — pipe flow — to a block profile. This introduces velocity components orthogonal to the flow direction, which in turn leads to the so-called die swell. Note that the orthogonal velocity component is orders of magnitude smaller than the velocity in the main flow direction.

Again, standard FEM and IGA computations were performed. For standard FEM, we utilized a Q1Q1 structured mesh with 86 by 16 nodes. For IGA, a NURBS of degree 2 with 86 by 16 control points was employed. In both cases, the time step was 0.015625. Note that in both cases, PDE-based displacement with the full velocity is not shown, as it is not usable for this application due to the strong tangential velocity component. The final meshes are given in Figure 15. Clearly, either of the proposed methods suitable in this case, retains good mesh quality.

Figure 16 plots the position of the corner node — as indicated in Figure 14 — over time. On the left, standard FEM results are displayed, on the right, the IGA results. All applied methods lead to nearly identical results. Thus, for this test case, no clear recommendation for any particular method can be given. However — as for the sloshing tank — the introduction of the PDE-based displacement methods allow for the usage of IGA.

6. Conclusion: Which mesh displacement method should be used?

The paper addresses options for interface tracking of free-surface problems. When considering boundary-conforming meshes in such a context, the adaptation of the boundary position — i.e., the boundary deformation — based on the flow field, or — more specifically — the no-penetration boundary condition, is

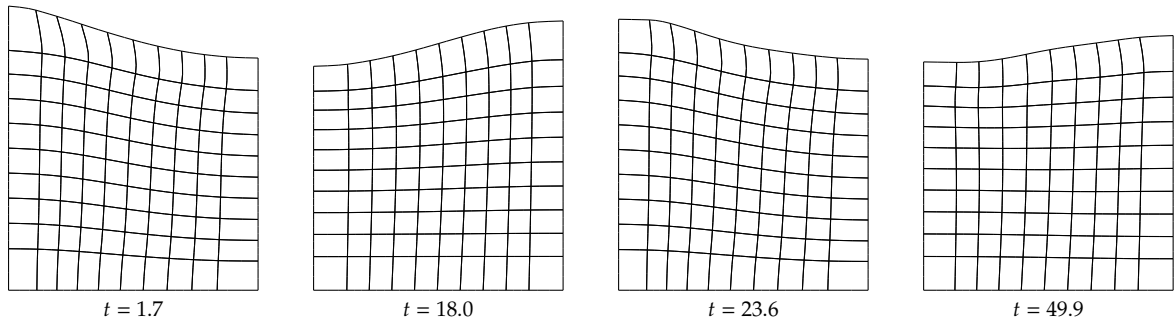


Figure 10: Element quality in physical space with Greville-based normal direction movement (12×12 control points, $\Delta t = 0.1$). The surface shows a kink.

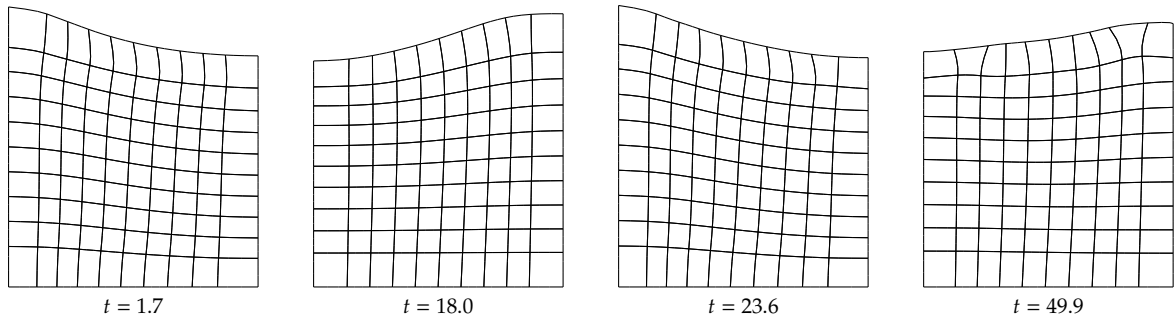


Figure 11: Element quality in physical space with PDE-based normal direction movement. The elements become distorted over time. (12×12 control points, $\Delta t = 0.1$).

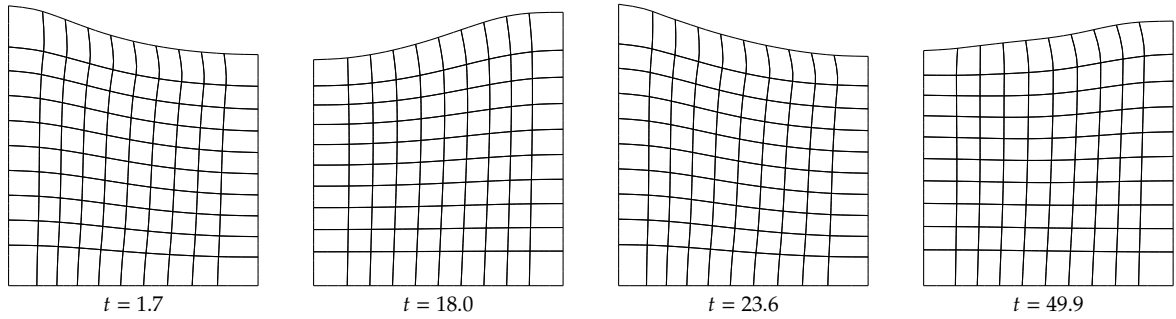


Figure 12: Element quality in physical space with PDE-based directional (vertical) movement. (12×12 control points, $\Delta t = 0.1$). The element quality remains high throughout the entire simulation.

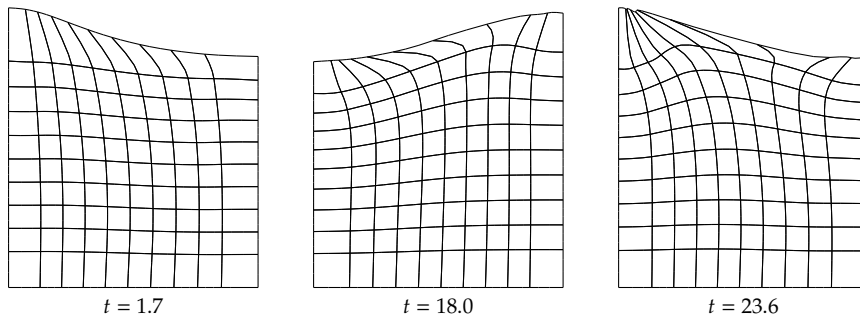


Figure 13: Element quality in physical space with PDE-based equal movement. (12×12 control points, $\Delta t = 0.1$). The elements become distorted over time.

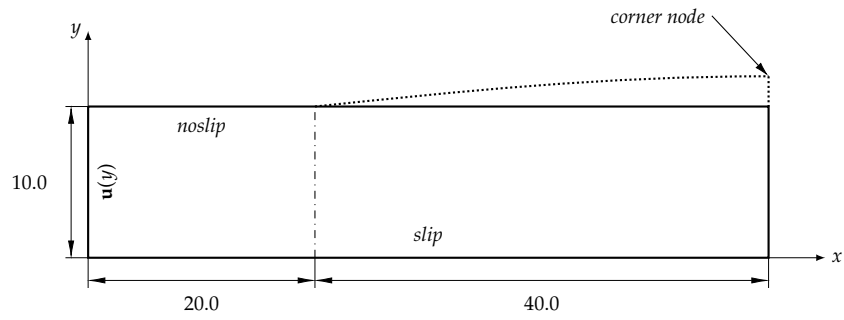


Figure 14: Die swell: test case setup. Velocity on left boundary $\mathbf{u}(y) = (0.1(100 - y^2), 0)^T$. Schematic quasi-steady solution shown by dotted line.

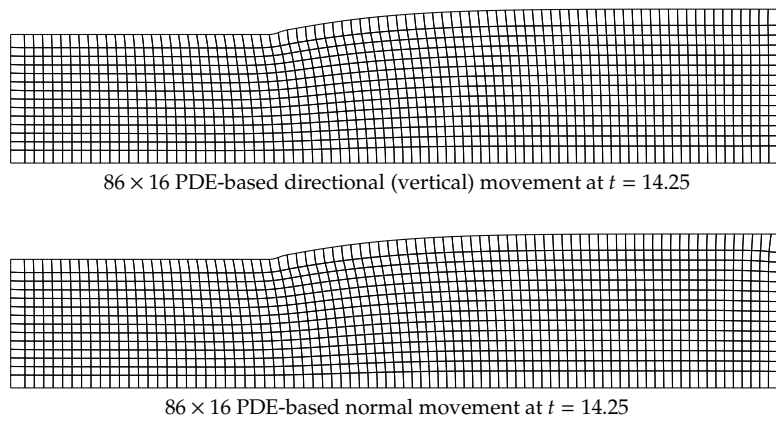


Figure 15: Meshes used for IGA simulations with $p = 2$. Elements are shown in physical space. While both meshes retain good quality, the directional movement seems to yield a better element shape in the upper right corner.

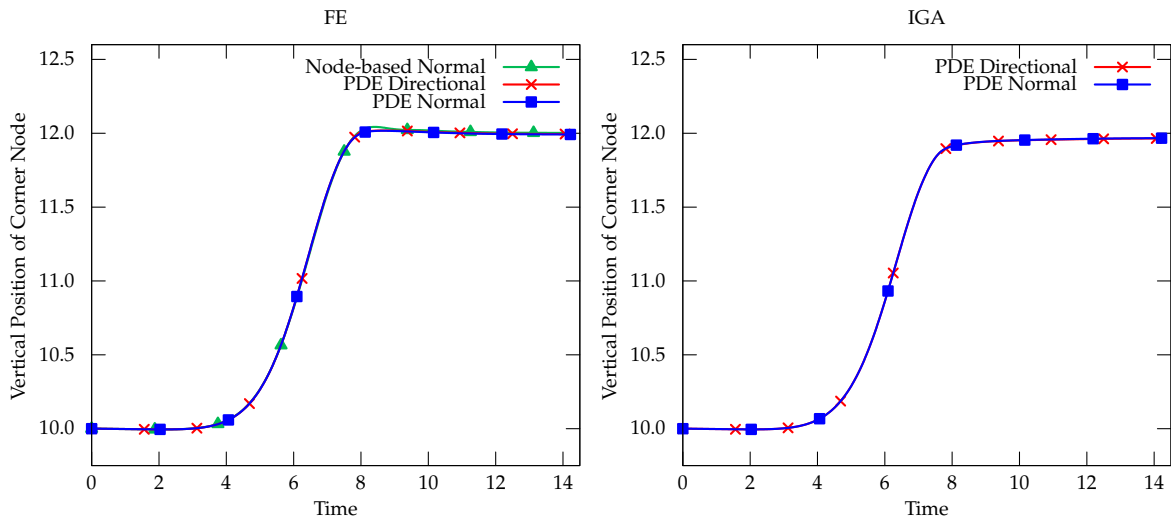


Figure 16: Comparison of node movement for FE and IGA

the major challenge. Motivated by the integral formulation of the no-penetration boundary condition, a PDE-based boundary displacement method is proposed. The new method has two significant advantages over the current state of the art: (1) It is applicable to finite element methods of linear and higher order as well as to isogeometric finite element methods, and (2) It guarantees mass conservation up to numerical errors caused by the solution process of the non-linear equation system, i.e., usually up to machine precision. In two space dimensions, the validity of the presented method has been confirmed with two standard numerical test cases for free-surface flow. The basic idea of the method is also applicable to three-dimensional problems.

Acknowledgments

The authors gratefully acknowledge the support of DFG under the Collaborative Research Center SFB 1120 (subproject B2) and DFG grant "Automated design and optimisation of dynamic mixing and shear elements for single-screw extruders" (EL 741/5-1).

References

- [1] S. Elgeti, H. Sauerland, Deforming Fluid Domains Within the Finite Element Method: Five Mesh-Based Tracking Methods in Comparison, *Archives of Computational Methods in Engineering* 23 (2) (2015) 323–361.
- [2] A. Caboussat, Numerical simulation of two-phase free surface flows 12 (2) (2005) 165–24.
- [3] C. R. Easton, Homogeneous Boundary Conditions for Pressure in the MAC Method 9 (1972) 375–379.
- [4] V. Girault, A Combined Finite Element and Marker and Cell Method for Solving Navier-Stokes Equations 26 (1976) 39–59.
- [5] J. Sethian, *Level Set Methods and Fast Marching Methods*, 2nd Edition, Cambridge University Press, 1999.
- [6] S. Osher, R. Fedkiw, Level set methods: An overview and some recent results 169 (2001) 463–502.
- [7] B. Nichols, C. Hirt, Improved free surface boundary conditions for numerical incompressible-flow calculations 8 (3) (1971) 434–448.
- [8] C. W. Hirt, B. D. Nichols, N. C. Romero, SOLA: A numerical solution algorithm for transient fluid flows, Tech. Rep. 32418, NASA STI/Recon Technical Report N 75 (1975).
- [9] W. Noh, P. Woodward, SLIC (Simple Line Interface Calculation), *Lecture Notes in Physics* 59 (1976) 330–340.
- [10] C. Hirt, B. Nichols, Volume of fluid (VOF) method for the dynamics of free boundaries 39 (1981) 201 – 225.
- [11] J. Gibbs, On the Equilibrium of Heterogeneous Substances, *Transactions of the Connecticut Academy of Arts and Sciences*, 1874-1878.
- [12] L. Onsager, Reciprocal Relations in Irreversible Processes, *Physical Review* 37 (405).
- [13] I. Prigogine, *Non-Equilibrium Statistical Mechanics*, 2nd Edition, Wiley, New York, 1966.
- [14] I. Gyrmati, *Non-Equilibrium Thermodynamics*, 1st Edition, Springer, New York, 1970.
- [15] S. de Groot, P. Mazur, *Non-Equilibrium Thermodynamics*, 1st Edition, Dover, New York, 1984.
- [16] H. Emmerich, *The Diffuse Interface Approach in Materials Science: Thermodynamic Concepts and Applications of Phase-Field Models*, Springer, 2003.
- [17] C. Hirt, A. Amsden, J. Cook, An arbitrary Lagrangian Eulerian computing method for all flow speeds 14 (1974) 227 – 253.
- [18] T. E. Tezduyar, M. Behr, J. Liou, A new strategy for finite element computations involving moving boundaries and interfaces—the deforming-spatial-domain/space-time procedure: I. the concept and the preliminary numerical tests 94 (3) (1992) 339 – 351.
- [19] E. Grotle, H. Bihs, E. P. an V. Aesoy, CFD Simulations of Non-Linear Sloshing in a Rotating Rectangular Tank Using the Level Set Method, in: *ASME 2016 35th International Conference on Ocean, Offshore and Arctic Engineering*, 2016.
- [20] J. Fonfach, T. Manderbacka, M. Neves, Numerical sloshing simulations: Comparison between lagrangian and lumped mass models applied to two compartments with mass transfer, *Ocean Engineering* 114 (2016) 168–184.
- [21] S. Elgeti, H. Sauerland, L. Pauli, M. Behr, On the usage of NURBS as interface representation in free-surface flows 69 (1) (2012) 73–87.
- [22] L. Pauli, M. Behr, S. Elgeti, Towards shape optimization of extrusion dies with respect to homogeneous die swell, *Journal of Non-Newtonian Fluid Mechanics* 69 (2012) 73–87.
- [23] A. Stavrev, P. Knechtges, S. Elgeti, A. Huerta, Space-time nurbs-enhanced finite elements for free-surface flows in 2d, *International Journal for Numerical Methods in Fluids* 81 (7) (2016) 397–459.
- [24] P. Knechtges, M. Behr, S. Elgeti, Fully-implicit log-conformation formulation of constitutive laws, *Journal of Non-Newtonian Fluid Mechanics* 214 (2014) 78–87.
- [25] P. Knechtges, The fully-implicit log-conformation formulation and its application to three-dimensional flows, *Journal of Non-Newtonian Fluid Mechanics* 223 (2015) 209–220.
- [26] M. Tomé, A. Castelo, V. Ferreira, S. McKee, A finite difference technique for solving the Oldroyd-B model for 3D-unsteady free surface flows, *Journal of Non-Newtonian Fluid Mechanics* 154 (2008) 179–206.
- [27] M. Tomé, A. Castelo, A. Afonso, M. Alves, F. Pinho, Application of the log-conformation tensor to three-dimensional time-dependent free surface flows, *Journal of Non-Newtonian Fluid Mechanics*.
- [28] G. Mompéan, L. Thais, M. Tomé, A. Castelo, Numerical prediction of three-dimensional time-dependent viscoelastic extrudate swell using differential and algebraic models, *Computers & Fluids* 44 (2011) 68–78.

- [29] G. Rocco, G. Coppola, L. de Luca, The VOF method applied to the numerical simulation of a 2D liquid jet under gravity, *WIT Transactions on Engineering Sciences* 69.
- [30] T. J. R. Hughes, J. A. Cottrell, Y. Bazilevs, Isogeometric analysis: CAD, finite elements, NURBS, exact geometry and mesh refinement 194 (2005) 4135–4195.
- [31] J. A. Cottrell, T. J. R. Hughes, Y. Bazilevs, *Isogeometric Analysis: Toward Integration of CAD and FEA*, John Wiley & Sons, Ltd, 2009.
- [32] H. Gómez, V. Calo, Y. Bazilevs, T. Hughes, Isogeometric analysis of the Cahn–Hilliard phase-field model 197 (49) (2008) 4333–4352.
- [33] M. Borden, J. Michael, C. Verhoosel, M. Scott, T. J. Hughes, C. Landis, A phase-field description of dynamic brittle fracture, *Computer Methods in Applied Mechanics and Engineering* 217 (2012) 77–95.
- [34] L. Dedè, M. Borden, T. Hughes, Isogeometric Analysis for Topology Optimization with a Phase Field Model 19 (2012) 427–465.
- [35] I. Akkerman, Y. Bazilevs, C. E. Kees, M. W. Farthing, Isogeometric analysis of free-surface flow, *Journal of Computational Physics* 11 (2011) 4137–4152.
- [36] R. Amini, R. Maghsoodi, N. Z. Moghaddamog, Simulating free surface problem using isogeometric analysis, *Journal of the Brazilian Society of Mechanical Sciences and Engineering* 38 (2) (2016) 413–421.
- [37] E. Rank, M. Ruess, S. Kollmannsberger, D. Schillinger, A. Düster, Geometric modeling, isogeometric analysis and the finite cell method, *Computer Methods in Applied Mechanics and Engineering* 249 (2012) 104–115.
- [38] A. Ginnisa, K. Kostasb, C. Politisb, P. Kaklisa, K. Belibassakisa, T. Gerostathisb, M. Scott, T. Hughes, Isogeometric Boundary-Element Analysis for the Wave-Resistance Problem using T-splines, *Computer Methods in Applied Mechanics and Engineering* 279 (2014) 425–439.
- [39] M. Behr, *Stabilized Finite Element Methods for Incompressible Flows with Emphasis on Moving Boundaries and Interfaces*, Ph.D. thesis, University of Minnesota, Department of Aerospace Engineering and Mechanics (1992).
- [40] A. Johnson, T. Tezduyar, Mesh update strategies in parallel finite element computations of flow problems with moving boundaries and interfaces 119 (1994) 73 – 94.
- [41] T. E. Tezduyar, M. Behr, S. Mittal, J. Liou, A new strategy for finite element computations involving moving boundaries and interfaces—the deforming-spatial-domain/space-time procedure: II. computation of free-surface flows, two-liquid flows, and flows with drifting cylinders 94 (3) (1992) 353 – 371.
- [42] T. Tezduyar, Computation of moving boundaries and interfaces and stabilization parameters, *International Journal for Numerical Methods in Fluids* 43 (2004) 555–575.
- [43] K. Takizawa, B. Henicke, T. Tezduyar, M.-C. Hsu, Y. Bazilevs, Stabilized Space–Time Computation of Wind-Turbine Rotor Aerodynamics, *Computational Mechanics* 48 (2011) 333–344.
- [44] K. Takizawa, T. Tezduyar, A. Buscher, S. Asada, Space-time interface tracking with topology change, *Computational Mechanics* 54 (2014) 955–971.
- [45] A. Zilian, A. Legay, The enriched space–time finite element method (est) for simultaneous solution of fluid–structure interaction, *International Journal for Numerical Methods in Biomedical Engineering* 75 (3).
- [46] M. Engelman, R. Sani, P. Gresho, The implementation of normal and/or tangential boundary conditions in finite element codes for incompressible fluid flow 2 (1982) 225–238.
- [47] L. Piegel, W. Tiller, *The NURBS Book*, Springer, Berlin, Germany, 1997.
- [48] D. Rogers, *An Introduction to NURBS with Historical Perspective*, Morgan Kaufmann Publishers, 2001.
- [49] Y. Bazilevs, V. Calo, J. Cottrell, J. Evans, T. Hughes, S. Lipton, M. Scott, T. Sederberg, Isogeometric analysis using T-splines 199 (2010) 229–263.
- [50] Y. Bazilevs, T. J. Hughes, Weak imposition of Dirichlet boundary conditions in fluid mechanics, *Computers and Fluids* 36 (2007) 12–26.
- [51] G. Farin, *Curves and Surfaces for Computer-Aided Geometric Design: A Practical Guide*, Elsevier, 2014.
- [52] A. Gray, *Modern differential geometry of curves and surfaces with Mathematica*, 2nd Edition, CRC Press, Boca Raton, 1998.